This paper appears in IEEE/ASME Transactions on Mechatronics
DOI: 10.1109/TMECH.2016.2598701

A Real-Time Estimator for Needle Deflection During Insertion Into Soft Tissue Based on Adaptive Modeling of Needle-Tissue Interactions

Thomas Lehmann[1], Carlos Rossa[1], Nawaid Usmani[2], Ron Sloboda[3] and Mahdi Tavakoli[1]

***Abstract*—This work proposes a real-time estimator for needle tip deflection and needle shape during needle insertion into soft tissue. The estimator is based on an adaptive quasi-static mechanics-based model for needle-tissue interactions. The model uses Euler-Bernoulli beam theory to model the needle as a cantilever beam that experiences loads imposed by the tissue. The modeled needle-tissue interactions consist of a distributed load along the inserted needle portion and tissue cutting-related point load at the needle tip. We propose a closed-form solution to quantify the magnitude of these needle-tissue interaction loads based on force and torque measured at the needle base. The model adaptively adjusts the shape of the distributed load as the needle is inserted. Experiments are carried out into gelatin phantom and porcine tissue to validate the deflection estimate's performance. The newly proposed model's performance is compared against a previously proposed quasi-static model for needle deflection estimation. It is shown that the novel model outperforms the previously proposed model.**

I. Introduction

Subcutaneous needle insertion is performed in several medical applications such as drug delivery, biopsy and radiation therapy. In interstitial prostate brachytherapy, radiation is administered internally by inserting radioactive seeds in and around the prostate in order to kill cancer cells in close proximity. These rice-grain sized seeds are inserted using hollow 18 gauge needles. The location of the seeds within the prostate is determined prior to the procedure in a pre-planning phase. Ideally, the seeds are placed equidistantly throughout the prostate in order to reach a consistent distribution of radiation for maximizing the treatment efficacy. Pre-planning is done based on the assumption that the needle remains on a straight path during insertion. Primarily due to the beveled tip of the needle, however, the needle deflects from its straight path during insertion [1], which causes seed misplacement and negatively affects treatment efficiency.

In current practice, the surgeon may manually correct for needle deflection by using strategies such as rotating the needle axially and applying lateral forces. Yet multiple needle retractions and re-insertions may sometimes be necessary to achieve a satisfactory needle trajectory, such that the seeds are placed close to their pre-planned location.

For keeping the needle on a straight path throughout insertion, robot-assisted needle insertion can be used. By rotating the needle axially by 180° at appropriate insertion depths, it can be steered towards a pre-defined target. Abolhassani *et al.* [2] showed that the needle deflection can be reduced by approximately 90% and Badaan *et al.* [3] showed that lesion targeting can be improved by 70% through axial rotation. For any on-line needle steering or control algorithm implemented in a robotic assistant system, needle deflection feedback is necessary. Other applications of needle deflection feedback are visual or haptic cues given to the surgeon during manual needle insertion in a surgeon-in-the-loop scenario [4] [5] [6]. The needle location inside tissue can be visualized in a virtual reality environment where the needle location is augmented onto the surgeon's field of view. Haptic feedback can be given to the surgeon in order to suggest corrective measures for the minimization of needle deflection in real-time.

Needle deflection feedback for control, prediction or deflection estimation is often obtained by directly measuring the needle deflection during insertion through imaging modalities such as ultrasound (US) or X-Ray [7]–[14]. These modalities are, however, limited in resolution, sampling rate, and the measurements are noisy. Furthermore, in a surgical scenario using US feedback, the US probe needs to be actuated such that it follows the needle tip accurately during insertion [12], [14], which limits the ability of the surgeon to observe desired prostate regions causing significant adjustment to the medical procedure.

Other solutions to estimate needle deflection are often sought in physically modeling the needle-tissue interactions in order to determine the resulting needle deflection from tissue loads imposed onto the needle. To this end, several needle-tissue interaction models based on mechanics and kinematics have been proposed [15]–[21]. Although most of these models have been shown to provide good needle deflection estimates, they require as input hard-to-characterize tissue parameters and geometric parameters of the needle such as the needle curvature resulting from deflection or needle cut angle.

A further direct approach for measuring the deflected needle shape, which has gained increasing popularity for the measurement of needle deflection are fiber Bragg grating (FBG) sensors [20]. FBG sensors are embedded in the needle shaft in order to measure the strain occurring as the needle bends

[1]Thomas Lehmann (Corresponding Author), Carlos Rossa and Mahdi Tavakoli are with the Department of Electrical and Computer Engineering, 11-203 Donadeo Innovation Centre for Engineering, 9211-116 Street NW, Edmonton, AB, Canada, T6G 1H9. E-mail: {lehmann, rossa, mahdi.tavakoli}@ualberta.ca

[2]Nawaid Usmani is with the Department of Oncology, Cross Cancer Institute, 11560 University Avenue, Edmonton, AB, Canada, T6G 1Z2. E-mail: nawaid.usmani@albertahealthservices.ca

[3]Ron Sloboda is with the Division of Medical Physics, Department of Oncology, Cross Cancer Institute, 11560 University Avenue, Edmonton, AB, Canada T6G 1Z2. E-mail: ron.sloboda@albertahealthservices.ca.

during insertion. A high sampling rate can be achieved with this sensing method. The needle, however, needs to house the fiber Bragg sensing units, which makes the method unsuitable for prostate brachytherapy as the hollow needle needs to contain radioactive seeds.

We introduce in this work a pseudo-static-model-based approach for estimating the needle tip deflection and the needle's shape during insertion into soft tissue. Our quasi-static, adaptive needle-tissue interaction model used to obtain the deflection estimate, is based on Euler-Bernoulli beam theory while the needle is modeled as a cantilever beam. Needle-tissue interactions are modeled by a distributed load acting along the inserted needle portion and a point load acting at the needle tip representing reaction forces caused by the cutting of tissue by the beveled needle tip.

The adaptive model component adjusts during insertion to the potentially changing load distribution due to non-homogeneous tissue. The unknown load parameters are found by relating them to the force and torque measured by a force/-torque sensor attached to the needle base. The measurements considered above can be obtained with a high sampling rate. In addition, the analytic solution of the differential equation governing the needle-tissue interactions make the model more computationally efficient than image-based needle tracking. Furthermore, our modeling approach does not need knowledge of tissue stiffness-related parameters, which would have had to be obtained prior to insertion. The model is therefore implicitly tissue independent.

The paper is organized as follows. Section II reviews prior research related to needle-tissue interaction and estimation of needle deflection, motivates and puts our deflection estimation approach into context. Section III introduces the model for interactions between needle and tissue. First, we introduce the load modeling approach for needle-tissue interactions, followed by the overall model combining the tissue reaction loads with the model of the needle. In Section IV, the needle-tissue interaction model is applied to estimating needle deflection and shape during insertion. Section V provides an experimental validation of the deflection estimate obtained. Results for deflection estimates during needle insertion are compared to measured deflections, and the overall performance of and possible improvements to the model are discussed.

II. Background & Motivation

Fig. **??** depicts schematically the clamped needle with modeled interaction loads during insertion. As the needle penetrates tissue, the needle tip cuts and causes tissue displacement, which in turn causes a reaction load enacted by the tissue onto the needle's bevel surface [15]. This load F_c is commonly modeled as a point load acting at the bevel surface's centre. Hence, the point load F_c, which will henceforth be referred to as the cutting force, is the initial cause for needle deflection.

As a result of its deflection, the needle applies lateral pressure onto the tissue along its inserted portion. The elastic properties of the tissue then cause the tissue to enact a reaction load onto the needle. This reaction is modeled as the distributed load $q_d(z)$ (see Fig. **??**). F_t is the vertical projection of the cutting force F_c. F_b and M_b are the base force and moment, which represent the reactions of the rigid needle clamping and can be measured by a force/torque sensor.

Several modeling approaches for force interactions between needle and tissue have been proposed for deflection estimation. Among those are mechanics-, Finite-Element-Method (FEM)-, kinematics- and statistics-based models.

Okamura *et al.* [15] investigated the types of force interactions occurring between the needle and tissue. The identified physical needle-tissue interactions are stiffness before puncture, friction and cutting force after puncture.

The first quasi-static mechanics-based needle-tissue interaction model [22] considers the tissue deformation as a uniform distribution along the inserted needle portion. The load is assumed to act in the same direction as the deflection and is caused by tissue displacement of the bevel tip. A model which establishes a relation between base force and the deflection is then derived. The model, however, underestimates needle deflection, which is attributed to the model underestimating needle bending outside of tissue. Using force interactions between needle and tissue such as cutting force and tissue support, and force/torque measurements at the needle base, Abolhassani *et al.* [2], [23] establish a relationship to needle deflection where a triangularly distributed load q_d, which weakens towards the needle tip, is assumed. It is presumed that the tissue acts as a support while the needle is pushed towards the direction of deflection during insertion. q_d is, however, not used in [2] for estimating the tip deflection since the load is assumed to be insignificantly small. Only considering a tip cutting force, however, contradicts the finding that the tip cutting force is constant [15] as the needle deflection increases with insertion depth.

Abayazid *et al.* [19] propose a mechanics-based model, in which a point load at the tip and a distributed load along the inserted portion of the needle are assumed. As in [2], the point load modeled at the needle tip is understood to be the tip cutting force. To further investigate the distributed needle-tissue interactions, Abayazid *et al.* [19] identified a load distribution shape along the inserted needle portion pre- and post rotation. In order to obtain the load distribution parameters, the difference between experimental deflection and simulated deflection is minimized. Thus, in order to parameterize the distributed load, pre-recorded experimental data is necessary. An error minimization approach between measured and simulated shape is utilized to identify the coefficients of the simulated polynomial shape.

Rossa *et al.* [12] describe a method to predict needle deflection based on the observation of deflection at a single point along the needle shaft via ultrasound images. The ultrasound probe can be maintained at the same position during insertion of the needle, which avoids complications of tissue deformation caused by the motion of the ultrasound probe. The method, however, relies on ultrasound feedback to predict needle deflection. Rossa *et al.* [14] present a model for needle deflection that adaptively updates the needle-tissue contact forces and tissue cutting force as a function of the tissue displacement along the needle shaft, based only on partial image feedback of the needle. Feedback is obtained by an

ultrasound probe that follows the needle tip and stops at an appropriate position to avoid further tissue displacement. Experimental results show an average error in predicting needle deflection of 0.36 mm. The deflection model takes as input the force at the needle tip and the tissue stiffness.

In Lehmann *et al.* [24], assumed needle-tissue interaction loads are parameterized using force and moment measurements at the needle base. Interaction loads along the needle are modeled with multiple distributed loads. Two triangularly distributed loads are considered to act along the needle shaft. The first load is shaped as a triangular load such that the maximum load intensity is at the entry point into tissue and with a decreasing intensity to zero at the needle tip. The load models tissue reacting to compression as the shaft moves laterally in the direction of deflection. The direction in which the load acts is therefore opposite the direction of deflection. The assumptions are the same as modeled in [2]. The second distributed load is also a triangularly distributed load with opposite direction and distribution intensity profile. The maximum force of distributed load two is at the needle tip and decreases towards the entry point. The second load assumption is based on the fact that the needle stores potential energy in its bent state, which results in a pressure applied onto the tissue in the upward direction, which in turn causes the tissue reaction pointing in the direction of deflection. The assumptions, however, do not take into account the force caused by the needle tip cutting tissue. In Lehmann *et al.* [25] the two triangular loads are replaced with a uniform load acting along the inserted needle portion and a point load enacted onto the needle tip. The uniform load also models tissue reacting to compression. The direction of the uniform load is therefore opposite to the direction of defection. The point load at the needle tip models the tissue cutting induced by the bevel.

An important limitation of [24] and [25] is that the distributed loads along the needle shaft are reduced to point loads. While reducing distributed loads to point loads is generally valid, calculating deflection based on the reduced loads causes inaccuracies. The results in both papers show an increasing error between tip deflection estimate and measured deflection with higher insertion depth. The new modeling approach presented in this work allows us to consider a distributed load along the needle shaft which, in contrast to our previous work, are not reduced to a single point load, which makes the model more precise as it can represent the reaction of tissue more accurately. The model is able to directly estimate the tip deflection and shape of the entire needle shaft during insertion. The formulation presented in [24] and [25] is primarily meant to estimate the tip deflection although it is possible to also estimate the needle shape in an additional step using the models with point load reduction.

Some of the above mentioned modeling methods also take tissue parameters as inputs, which are typically hard to characterize. Since our approach only needs force and moment measurements at the needle base to parameterize the needle-tissue interaction model, the method is independent of tissue parameters.

The goal is also to further enhance the deflection estimate capability over a range of tissue stiffness and inhomogeneities while only considering measurements such as force and moment at the needle base as model input. To this end, a differential equation based on Euler-Bernoulli beam theory is used to represent the static system of the clamped needle, which is subject to the modeled tissue loads. This equation is then integrated four times in order to obtain a closed form solution of shear force, bending moment, slope and finally deflection at any point along the needle. The following section introduces the model.

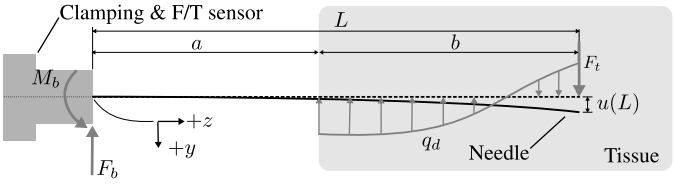

Fig. 1. The needle and applied tissue reactions modeled as a distributed load q_d and point load F_t. L is the needle length, a and b are the needle portions outside and inside of tissue, respectively. M_b and F_b represent moment and force, respectively, measured at the needle base.

III. An Adaptive, Quasi-Static Model for Needle-Tissue Interactions

This section introduces the formulation for the needle-tissue interactions during insertion into tissue. The model is then used in Section IV to obtain an estimate of the needle deflection.

A. Modeling of Interaction Loads

The needle-tissue interactions, which cause the needle deflection shape, are represented as a distributed load q_d along the inserted needle portion and a point load F_t at the needle tip as depicted in Section II and Fig. 1. Both q_d and F_t are discontinuous in space. q_d only acts where the needle is surrounded by tissue and is therefore modeled as a discontinuity at the needle entry point into tissue. A widely used method to model loads of this kind involves singularity functions [26], i.e.,

$$q(z) = \frac{q_0}{b^n}\langle z-a\rangle^n; \quad n = 0,1,2,... \tag{1}$$

with

$$\langle z-a\rangle^n = \begin{cases} 0 & \text{when } z \le a \\ (z-a)^n & \text{when } z > a \\ +\infty & \text{when } z = a \\ 0 & \text{when } z \ne a \end{cases} \quad \begin{matrix} \text{if } n = 0,1,2,... \\ \\ \\ \text{if } n = -1 \end{matrix} \tag{2}$$

where a is the shift from zero.

1) Distributed load q_d: Four examples of loads, which can be modeled with the above approach are shown in Fig. 2. The mathematical forms associated to the load examples are $F\langle z-L\rangle^{-1}$ for Fig. 2a, $\frac{q_0}{b^0}\langle z-a\rangle^0$ for Fig. 2b, $\frac{q_0}{b^1}\langle z-a\rangle^1$ for Fig. 2c and $\frac{q_0}{b^2}\langle z-a\rangle^2$ for Fig. 2d with the loads being shifted about a. The maximum load intensity q_0 acts at a point $z > a$. The parameter b refers to the distance from point $z = a$ at which the value q_0 is defined.

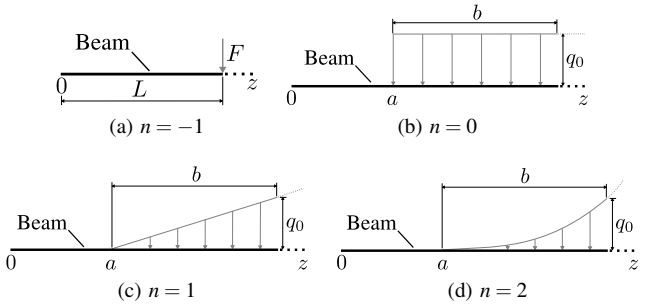

Fig. 2. A schematic representation of (a) a point load, (b) a uniform, (c) a triangular and (d) a parabolic load distribution. a is the shift from zero and q_0 is the load magnitude at the variable distance z along the beam.

More complex polynomial load shapes of any order m can be formulated as superpositions of (1):

$$q(z) \quad = \quad \sum_{i=0}^{m} \frac{q_i}{b^i} \langle z-a \rangle^i \tag{3}$$

where q_i is the magnitude of the load expressed by the i^{th} term at z. When (3) is used to model the distributed load q_d along the inserted needle portion as illustrated in Fig. 1, a becomes the portion of the needle outside tissue, and b represents the needle portion inside tissue. The general formulation for q_d in (3) is advantageous as any polynomial shape can be modeled. The integrability of (3) is later used to derive the analytic solution to the beam deflection formulation, which models needle deflection.

2) Point load F_t: As F_t acts as a point load, it is naturally also not continuous and is commonly modeled as a shifted Dirac delta function. The point load F_t related to the cutting force F_c at $z=L$, the needle tip, is modeled as

$$q_t(z) \quad = \quad F_t \langle z-L \rangle^{-1}. \tag{4}$$

B. The Needle-Tissue Interaction Model

The needle is modeled as a cantilever beam, which is subject to the above described loads. Euler-Bernoulli beam theory is used to obtain a governing equation for the needle-tissue system. The resulting equation is a fourth-order ordinary differential equation (ODE). The right hand side of the ODE consists of the applied loads enacted by tissue onto the needle. The analytic formulation for the needle deflection is derived in the following.

The ODE governing the needle-tissue system is

$$\begin{aligned} \frac{d^2}{dz^2}\left(EI\frac{d^2u}{dz^2}\right) &= q_d(z)+q_t(z) \\ &= \sum_{i=0}^{m} \frac{q_i}{b^i}\langle z-a\rangle^i + F_t\langle z-L\rangle^{-1} \end{aligned} \tag{5}$$

where u is the needle deflection along the y-axis (see Fig. 1), E is the needle's Young's modulus and I is the needle's area moment of inertia. In order to obtain the deflection u, which results from the applied loads $q_d(z)$ and $q_t(z)$, (5) is integrated four times with respect to z. The first integration of (5) gives the shear force $V(z)$ along the needle:

$$\begin{aligned} -V(z) &= \frac{d}{dz}\left(EI\frac{d^2u}{dz^2}\right) = \int q_d(z)+q_t(z)\,dz \\ &= \sum_{i=0}^{m} \frac{q_i}{b^i(i+1)}\langle z-a\rangle^{i+1} + F_t\langle z-L\rangle^0 + C_1. \end{aligned} \tag{6}$$

The boundary condition used to obtain the integration constant C_1 in (6) is the shear force at the needle tip ($z=L$) being equal to zero. Therefore, $V(L)=0$ and

$$-V(z) = \sum_{i=0}^{m} \frac{q_i}{b^i(i+1)}\langle z-a\rangle^{i+1} - \underbrace{b\sum_{i=0}^{m}\frac{q_i}{(i+1)}}_{d_1} - F_t. \tag{7}$$

Integration of (7) gives the bending moment $M(z)$ along the needle:

$$\begin{aligned} -M(z) &= EI\frac{d^2u}{dz^2} \\ &= \sum_{i=0}^{m} \frac{q_i}{b^i\prod_{j=1}^{2}(i+j)}\langle z-a\rangle^{i+2} - d_1 z - F_t z + C_2 \end{aligned} \tag{8}$$

where d_1 is the second summation term as shown in (7). The boundary condition used to obtain the integration constant C_2 in (8) is the bending moment at the needle tip ($z=L$). The boundary condition is known to be zero. Therefore $M(L)=0$ and

$$\begin{aligned} -M(z) = &\sum_{i=0}^{m} \frac{q_i}{b^i\prod_{j=1}^{2}(i+j)}\langle z-a\rangle^{i+2} - d_1(z-L) \\ &\underbrace{-b^2\sum_{i=0}^{m}\frac{q_i}{\prod_{j=1}^{2}(i+j)}}_{d_2} + F_t(L-z) \end{aligned} \tag{9}$$

The sign conventions in the above equations for the shear force $-V(z)$ and bending moment $-M(z)$ are according to Gere *et al.* [26, p. 463f]. Shear force $V(z)$ and bending moment $M(z)$ are negative in case of a positive deflection because the z axis is positive rightward and the y axis is positive downward. The angle θ is positive when clockwise.

Dividing (9) by EI and integrating once with respect to z gives the deflection slope $\theta(z)$ along the needle. The needle is clamped at its base, which means that $\frac{du}{dz}\big|_{z=0}=0$. Hence, the boundary condition for $\theta(z)$ is $\theta(0)=0$. Therefore,

$$\begin{aligned} \theta(z) = \frac{du}{dz} = \frac{1}{EI}\Bigg[&\sum_{i=0}^{m}\frac{q_i}{b^i\prod_{j=1}^{3}(i+j)}\langle z-a\rangle^{i+3} \\ &-\frac{d_1}{2}z^2 - (d_2-d_1L)z + \frac{F_t z}{2}(2L-z)\Bigg] \end{aligned} \tag{10}$$

where d_2 is the second term in (9).

By integrating (10), the beam deflection is obtained. The boundary condition for $u(z)$ is $u(0)=0$. Therefore,

$$\begin{aligned} u(z) = \frac{1}{EI}\Bigg[&\sum_{i=0}^{m}\frac{q_i}{b^i\prod_{j=1}^{4}(i+j)}\langle z-a\rangle^{i+4} - \frac{d_1}{6}z^3 \\ &-\frac{1}{2}(d_2-d_1L)z^2 + \frac{F_t z^2}{6}(3L-z)\Bigg] \end{aligned} \tag{11}$$

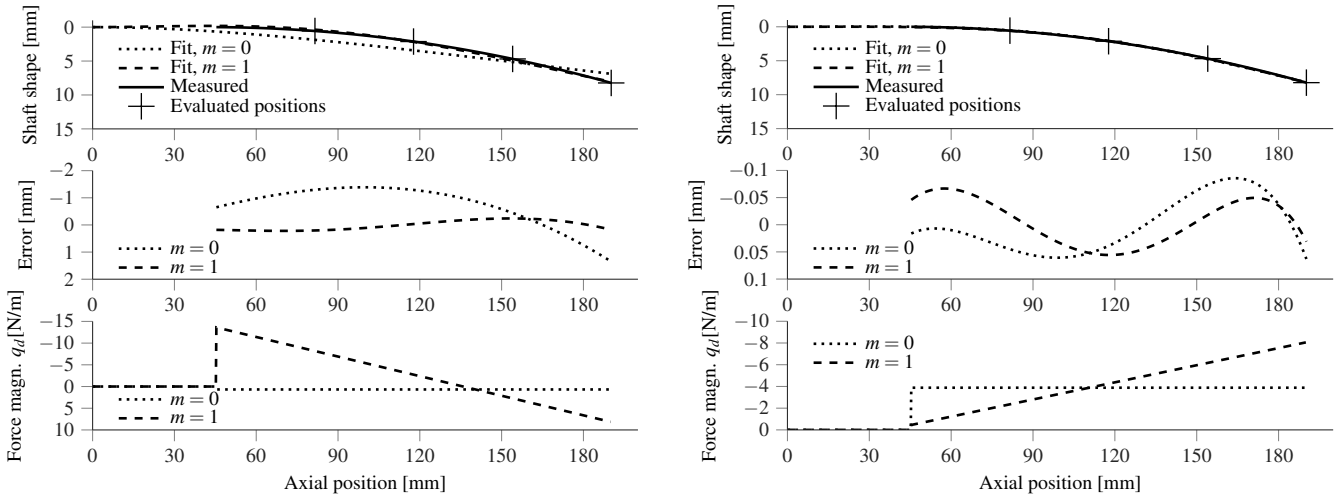

Fig. 3. The optimization result with $m=0$ and $m=1$, insertion velocity 5 mm/s and Tissue 1. Optimization results (a) without considered F_t and (b) with considered F_t. The middle plots shows the error between measured and fit shape. The identified load parameters shown in the bottom plot of (a) are $\mathbf{q}=[0.67]$ N/m for $m=0$ and $\mathbf{q}=[-13.64\ \ 21.78]$ N/m for $m=1$, and (b) are $\mathbf{q}=[-3.88]$ N/m and $F_t=0.33$ N for $m=0$ and $\mathbf{q}=[-0.45\ \ -7.61]$ N/m and $F_t=0.44$ N for $m=1$.

where d_1 and d_2 are defined in (7) and (9), respectively. The following section uses the model introduced in this section to devise a method for estimating needle deflection in real-time.

IV. Real-Time Deflection Estimator

This section introduces a method to estimate the magnitudes of the loads, which are later used in (11) to find the needle deflection $u(z)$. In order to obtain $u(z)$ using (11), first the load parameters q_i and F_t need to be found. In the model, the parameters m, q_i and F_t define the shape and magnitudes of the loads applied onto the needle. m is the polynomial order of the distributed load q_d along the inserted needle portion. Thus, m determines how many iterations of the load components shown in Fig. 2 must be superimposed.

The question now arises which polynomial order and thus how many measurements are necessary to obtain an accurate needle deflection estimate. In other words, we need to determine how many load components must be superimposed according to (11) in order to accurately predict needle deflection. The following section addresses this question and gives an analysis with regards to different considered load shapes.

A. Identification of Load Shape

We want to estimate the needle deflection with only the two measurements force and torque at the needle base with an analytic approach. Here we show that this can be done with a sufficient accuracy.

The procedure is divided into two steps: 1) minimization of a cost function involving the residual between estimated and measured shape of the needle shaft. Four measurements along the deflected needle shaft at the final insertion depth are used in a cost function, which takes the load parameters. In step 2), multiple iterations of this optimization algorithm while incrementing m in each iteration are performed. A comparison of the mean absolute error (MAE) between the measured and estimated needle shaft shape for different m reveals the necessary minimum order for $q_d(z)$.

Step 1: A cost function is devised, which determines the residual R between estimated and measured needle shaft shape at the final insertion depth. Measured shape $u(\mathbf{z})$ with $\mathbf{z}=[82,118,154,190]$ mm is acquired from the same experimental data as described in Section V. The estimated shape $\hat{u}(\mathbf{z})$ is obtained from (11). R is minimized by optimizing the selection of the load parameters $\mathbf{q}=[q_0,q_1,...,q_i,...,q_m]$ and F_t. The cost function is

$$R(\hat{\mathbf{q}},\hat{F}_t)=\left(\sum_{j=1}^{4}\left|\hat{u}(\mathbf{z}_j,\hat{\mathbf{q}},\hat{F}_t)-u(\mathbf{z}_j)\right|^2\right)^{1/2} \tag{12}$$

where $\hat{\mathbf{q}}=[\hat{q}_0,\hat{q}_1,...,\hat{q}_i,...,\hat{q}_m]$ is the vector of parameter estimates for the distributed load $q_d(z)$, $\hat{F}_t$ is the parameter estimate for the point load magnitude and j is the component index of $\mathbf{z}$.

To fit the measured shape to the estimated shape through optimizing $\hat{\mathbf{q}}$ and $\hat{F}_t$, R is minimized via MATLAB®'s *GlobalSearch* class with `fmincon` chosen as solver.

Step 2: To identify m, *Step 1* is carried out multiple times while m is incremented starting from zero in each iteration. Two different scenarios are considered. The first scenario includes the load F_t and in the second scenario, F_t is set to zero. We expect the distributed load q_d to change accordingly if F_t is omitted to incorporate the needle tip's cutting force. The reason for considering the second scenario is that the amount of required load parameters is reduced by one while the needle-tissue interaction load modeling still closely resembles the physical needle-tissue interactions.

Fig. 3 shows plots of two estimated ($m=0$ & $m=1$) versus the measured needle shaft shape at the final insertion depth b of 140 mm at an insertion velocity of 5 mm/s for Tissue 1 (see Section V). In Fig. 3a, F_t is omitted while in Fig. 3b, F_t is used

TABLE I
THE OPTIMIZATION PERFORMANCE FOR DIFFERENT m MEASURED IN MAE FOR INSERTION VELOCITY 5 MM/S. σ IS THE STANDARD DEVIATION OF THE ERROR BETWEEN MEASUREMENT AND ESTIMATE.

m	Tissue 1 MAE [mm]	Tissue 1 σ [mm]	Tissue 2 MAE [mm]	Tissue 2 σ [mm]	Considered load parameters
0	0.042	0.048	0.070	0.082	q_0, F_t
1	0.037	0.041	0.074	0.094	q_0, q_1, F_t
2	0.031	0.031	0.024	0.034	q_0, q_1, q_2, F_t
0	0.957	0.726	1.175	0.886	q_0
1	0.155	0.169	0.142	0.160	q_0, q_1
2	0.071	0.075	0.128	0.145	q_0, q_1, q_2

during parameter fitting. The plots illustrate the optimization performance for different m and the two considered scenarios. It can be observed that q_d adjusts accordingly when F_t is omitted.

Table I contains the error between the measured and estimated needle shaft shape expressed as MAE at insertion depth b =140 mm for insertion velocity 5 mm/s and two Gelatin tissue samples (Tissue 1 and Tissue 2) with different stiffness (see Section V). The data shows that case $m = 1$ with omitted F_t and case $m = 0$ with considered F_t both show a small MAE $\ll 1$ mm. Therefore, both of the above cases need to be considered for force/torque based deflection estimation. It can also be concluded that only two measurements are necessary for obtaining an accurate needle shape and tip deflection estimate, which is helpful for the following section.

B. Force-Sensor-Based Deflection Estimation

To find the deflection estimate analytically, two measurements are assembled into a system of two equations. As measurements, we use the force and torque measured at the needle base by a force/torque sensor. The base forces/torque measurements are the shear force and bending moment, respectively, at $z = 0$. Hence, for example, in order to obtain the two load parameters $\mathbf{q} = [\, q_0 \;\; q_1 \,]^T$, the following system of equations, consisting of (7) and (9) is solved for

$$\underbrace{\begin{bmatrix} q_0 \\ q_1 \end{bmatrix}}_{\mathbf{q}} = \mathbf{C}^{-1} \underbrace{\begin{bmatrix} V(0) = F_b \\ M(0) = M_b \end{bmatrix}}_{\mathbf{m}} \tag{13}$$

with

$$\mathbf{C} = \begin{bmatrix} b & b/2 \\ b(-L+b/2) & b/2(-L+b/3) \end{bmatrix}$$

where $\mathbf{m} = [\, F_b \;\; M_b \,]^T$ is the vector of measurements. To obtain the deflection estimate $\hat{u}(z)$ at the current insertion depth b for $z \in (0, L)$, load parameters $\mathbf{q}$ obtained from (13) are inserted into (11). Then the deflection $u(z)$ expressed as a function of the measurements is

$$\hat{u}(z, \mathbf{q}) = \frac{1}{EI} \left[\sum_{i=0}^{1} \frac{\mathbf{q}_{i+1}}{b^i \prod_{j=1}^{4} (i+j)} \langle z-a \rangle^{i+4} - \frac{d_1}{6} z^3 - \frac{1}{2} (d_2 - d_1 L) z^2 \right] \tag{14}$$

with $d_1 = b \sum_{i=0}^{1} \frac{\mathbf{q}_{i+1}}{i+1}$ and $d_2 = b^2 \sum_{i=0}^{1} \frac{\mathbf{q}_{i+1}}{\prod_{j=1}^{2} (i+j)}$.

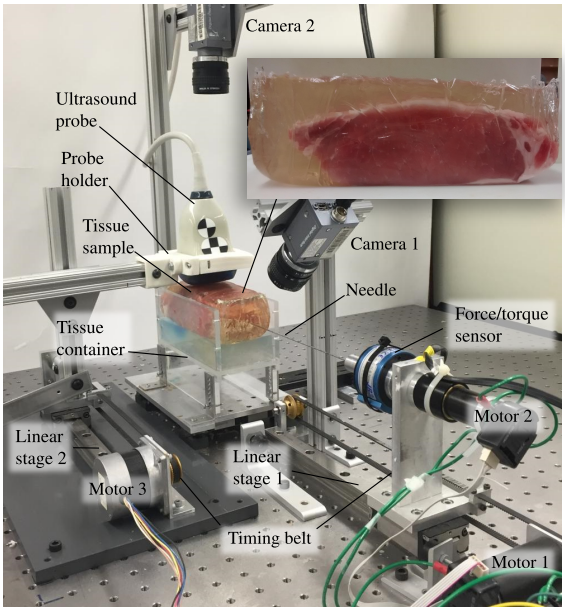

Fig. 4. The experimental testbench for performing needle insertions. A DC motor (Motor 1) provides the linear motion to insert the needle into the tissue. A second motor (Motor 2) attached to the needle base rotates the needle around its axis during insertion (not used in this paper). A stepper motor (Motor 3) provides linear motion for the ultrasound probe. The forces at the needle base are measured by a force/torque sensor. Images of the needle inside tissue are recorded by Camera 2. Camera 1, which records close-up images of the needle at its entry point into tissue, is not used.

V. EXPERIMENTAL VALIDATION

This section presents the experimental validation of the model-based quasi-static needle deflection estimation approach introduced in Section III and Section IV.

A. Experimental Setup

The experimental testbench used to perform repeatable needle insertion experiments into soft phantom tissue is the 2-DOF prismatic-revolute robotic system shown in Fig. 4. The needle, which represents the end-effector of the robot, can be translated along and rotated about its longitudinal axis. The translational motion is guided by a linear stage coupled to a timing belt, which is driven by a DC motor (RE40, Maxon Motor AG, Sachseln, Switzerland). The rotational motion is not used during the experiments presented in this work. The rotational motor's shaft carries a 6 DOF force/torque transducer (50M31A3-I25, JR3 Inc., Woodland, CA, USA) to record the force and torque that are the model inputs. The sensor's remaining recordings are not used. Since the sensor measures moments around its center and the bending moments of interest are the ones occurring at the needle clamping's tip, the measured moments need to be re-calculated to account for the length of the clamping: $M_b = M_s - F_b c$ where M_s is the measured force, and $c = 52.75$ mm is the distance between the sensor's center and the needle clamping's tip. Constant velocity insertions are facilitated using a PID controller. For real-time control and data acquisition, Simulink Real-Time™ (MathWorks® Inc., Natick, MA, USA) is used.

Fig. 4 also depicts a camera mounted above the tissue container (Camera 2) and an actuated US probe mounted above

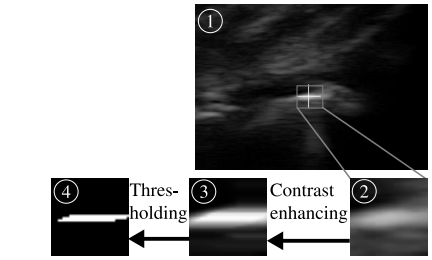

(a)

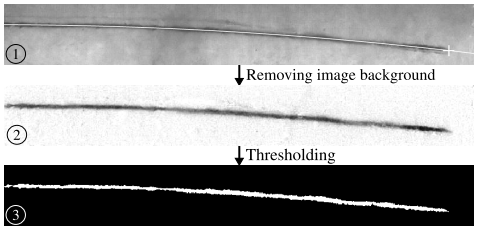

(b)

Fig. 5. Needle deflection measurement in (a) axial ultrasound images and (b) camera images.

the tissue sample. Camera 2 captures images from a total perspective of the inserted needle portion in order to observe the needle shape and tip position during insertion.

The US probe (4DL14-5/38 Linear 4D, Ultrasonix, Richmond, BC, Canada) is mounted onto a crossbar structure by the probe holder and is connected to Linear stage 2, which allows for the probe to be translated along the length of the tissue container. Linear stage 2 and thus the US probe is actuated by a stepper motor (Motor 3) via a timing belt. A diagnostic US system (SonixTOUCH, Ultrasonix, Richmond, BC, Canada) is used to generate US images from the sonography data acquired by the US probe.

B. Needle Deflection Measurement

For validation of the needle deflection estimation, the needle shape and tip deflection are measured based on images during insertion into phantom and biological tissue. For the transparent phantom tissue, camera images acquired from Camera 2 are used to measure needle tip deflection and needle shape. The US probe is removed for experiments involving Camera 2. For experiments with non-transparent biological tissue US images are acquired to measure needle tip deflection and shape.

During needle insertion, the position of the US probe is controlled such that it tracks the needle tip. A proportional controller minimizes the relative distance between the needle tip and the probe during insertion. Fig. 5a, image 1 shows a sample US image. Within the image, a region of interest (ROI) is marked around the bright spot representing the needle cross-section (see Fig. 5a, image 2). The white cross within the ROI indicates the needle position detected by the algorithm described in [11]. In Fig. 5a, images 2, 3 and 4 illustrate the sequence of image processing applied by the algorithm in order to extract the needle cross-section. Before insertion is started, the initial ROI position is supplied by the user. In each subsequent US image, the ROI position is chosen

Algorithm 1 Needle shape & tip position measurement

```
function PROCESS_IMAGES(img_set)
    for i = 1 to len_img_set do
        Removing image background:
        img_diff ← img_set(i) - img_set(1)
                    ▷ Take difference between current & initial image
        thres ← max(img_noise) + ε
        img_bw ← im2bw(img_diff, thres)
                                        ▷ Convert to binary image
        Obtaining needle shape:
        pnt_cloud ← img_bw
                    ▷ Convert img_bw (needle contour) to point cloud
        p_coef ← polyfit(pnt_cloud,2)
                                ▷ Fit polynomial to pnt_cloud
        Detecting needle tip position:
        x ← 0
                                                ▷ Init image column counter
        win ← ones(len_win, 1)
                                                    ▷ Init window win
        thres_sum ← len_win * 0.05
        while sum(win) > thres_sum do
            x++
            y ← polyval(p_coef, x)
            win ← [img_bw(y,x) win(1:len_win-1)]
                            ▷ Move win one horizontal pixel forward
        end while
        array_pos_tip(i,:) ← [y x]
    end for
    return array_pos_tip
end function
```

around the detected needle position in the previous image. Next, the algorithm uses an Intensity Transform to enhance the image contrast (see Fig. 5a, image 3). This is followed by the identification and application of a threshold on the ROI to obtain a binary image containing a blob representing the needle cross-section (see Fig. 5a, image 4). The centre point of the cross-section is finally found by taking the horizontal and vertical median of image 4. The RANSAC and Anisotropic Diffusion components considered in [11] are not used in this work. The millimeter-to-pixel ratio for US images is 0.064 mm/pixel. When the insertion robot reaches the final insertion depth and after insertion is stopped, the US probe is moved back with a constant velocity to its initial position in order to capture the needle's *shape* inside tissue.

Images of the needle inside phantom tissue are continuously taken throughout insertion at two different locations by two SONY XCD-SX90CR cameras (Sony Corporation, Tokyo, Japan). Algorithm 1 illustrates the method for needle shape and tip deflection measurement.

Fig. 5b shows three images depicting the extraction of the needle contour. In image 1, the fit needle shape and the measured tip position are shown by a line and cross, respectively. Image 2 corresponds to `img_diff` and image 3 corresponds to `img_bw` as described in Algorithm 1. The millimeter-to-pixel ratio for Camera 2 is 0.192 mm/pixel.

In order to find the needle shape in the images acquired by Camera 2, the needle contour is first extracted from the image background (initial image, `img_set(1)`). The fact that no needle is present in the initial frame is exploited to remove the background from a frame with needle by subtracting the initial frame from the current frame. A threshold is applied onto the differential image to obtain a binary image `img_bw` of the needle contour. `img_bw` is then converted into a point

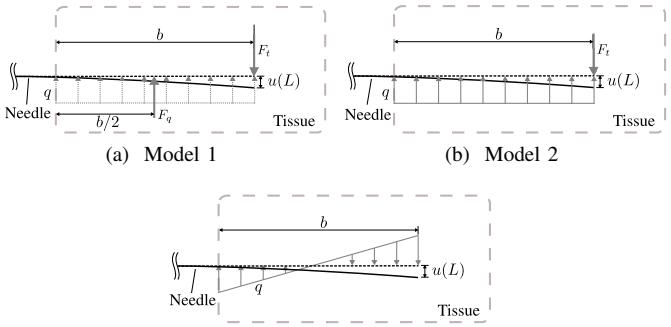

(a) Model 1 (b) Model 2

(c) Model 3

Fig. 6. The model variants considered for performance analysis. (a) Model 1: Introduced in [25]. The uniformly distributed load is reduced to the point load F_q. (b) Model 2: The uniformly distributed load is not reduced to a point load. (c) Model 3: A superposition of a uniform and triangular load ($m = 1$).

cloud and a polynomial is fit onto the points by using a least-squares approach. To find the needle tip, a window (`win`) of a pre-defined length is moved along the polynomial fit in the binary image `img_bw`. The tip is detected when the amount of pixels in `win` with value 1 is smaller than a pre-defined threshold, meaning that the needle's distal end has been reached.

C. Experimental Results

Needle insertion experiments into phantom tissue made from gelatin (Knox®, NBTY Inc., Ronkonkoma, NY, USA) and porcine tissue are carried out with a standard hollow 18G (⌀ 1.27 mm) brachytherapy needle (Eckert & Ziegler BEBIG Inc., Oxford, CT, USA), which has a length of 200 mm and is made from stainless steel. The effective needle length is, however, 190 mm due to the clamping at the needle's base. The insertion velocity is kept constant at 5 mm/s and the final insertion depth is 140 mm. The deflection measurements obtained based on images from these insertions serve as the ground truth for model performance analysis.

Needles are inserted into two phantom tissue samples, Tissue 1 and Tissue 2, made with a gelatin to water ratio of 160 g/l and 194 g/l, respectively. This results in a significantly different tissue stiffness. The stiffness, estimated through indentation tests, is approximately 45 kPa for Tissue 1 and 60 kPa for Tissue 2. The values found for the two phantom tissues are similar to the properties of animal tissue [27]. Moreover, insertions into a sample of porcine loin muscle tissue, Tissue 3, are carried out. The porcine tissue sample is embedded into gelatin with a gelatin to water ratio of 150 g/l. A picture of the porcine tissue sample is given in Fig. 4. Needles are inserted from the left hand side into the sample. Six insertion trials are performed into each of the three tissue samples while a new location is chosen for each insertion. Thus in total, 18 insertions are carried out. Prior to the start of each insertion, the needle is inserted 10 mm into phantom tissue and 15 mm into porcine tissue, respectively. This is done to ensure that the needle is visible in the initial US image.

The deflection estimation performance of two variants of the model introduced in this work and a comparable quasi-static model presented in [25], as shown in Fig. 6, are compared in Fig. 7.

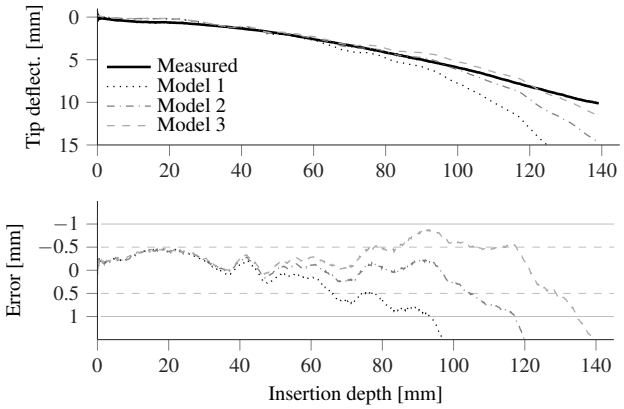

(a) Tissue 1

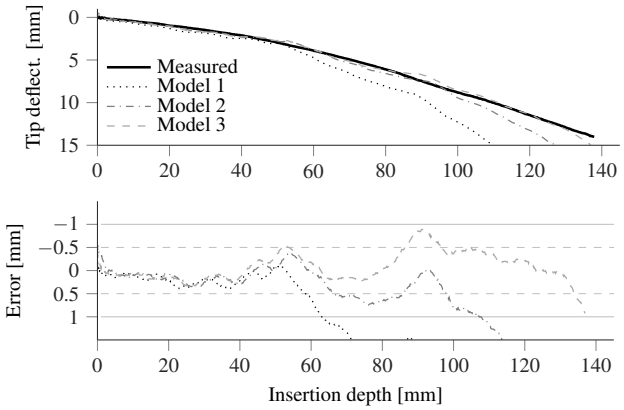

(b) Tissue 2

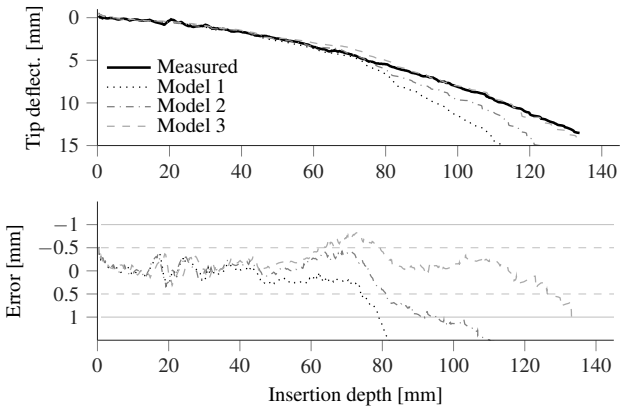

(c) Tissue 3

Fig. 7. The average of six insertion trials is plotted for estimated and measured tip deflection for three quasi-static model variants (Model 1, Model 2 and Model 3) for Tissue 1 (a), Tissue 2 (b) and Tissue 3 (c). The bottom plot contains the error between measured and estimated deflection for all three models.

- Model 1 (see Fig. 6a) models needle-tissue interactions as a uniformly distributed load along the inserted needle portion, which is reduced to a point load acting at the distributed load's center of gravity, and a point load at the needle tip related to cutting force. The model was presented in [25] and shown to be the best performing

TABLE II
RESULTS OF A TWO-SAMPLE t-TEST. MEASURED AND ESTIMATED TIP DEFLECTION MEANS OVER 6 TRIALS ARE COMPARED.

Tissue #	Model #	Insertion depth [mm]			
		34.5	69	103.5	138
1	1	$\bar{r}$	$\bar{r}$	r	r
	2	$\bar{r}$	$\bar{r}$	$\bar{r}$	r
	3	$\bar{r}$	$\bar{r}$	$\bar{r}$	$\bar{r}$
2	1	$\bar{r}$	$\bar{r}$	r	r
	2	$\bar{r}$	$\bar{r}$	$\bar{r}$	r
	3	$\bar{r}$	$\bar{r}$	$\bar{r}$	$\bar{r}$
3	1	$\bar{r}$	$\bar{r}$	r	r
	2	$\bar{r}$	$\bar{r}$	$\bar{r}$	r
	3	$\bar{r}$	$\bar{r}$	$\bar{r}$	$\bar{r}$

r denotes that the null hypothesis must be rejected and $\bar{r}$ denotes that it can not be rejected at the 5% significance level.

TABLE III
THE MEAN ABSOLUTE ERROR BETWEEN MEASURED AND ESTIMATED TIP PATH FOR ALL TISSUE SAMPLES AND MODELS IN MILLIMETERS.

Tissue #	Mean absolute error [mm]		
	Model 1	Model 2	Model 3
1	1.90	0.68	0.40
2	2.30	0.79	0.26
3	2.23	0.84	0.26

model among two other evaluated models during insertion into agar phantom tissue samples.

- Model 2 (see Fig. 6b) is based on the methodology introduced in this work. Needle-tissue interactions are modeled as a uniformly distributed load ($m = 0$) and a point load at the needle tip. The model inputs are needle base force/torque measurements.
- Model 3 (see Fig. 6c) is also based on the methodology introduced in this work. It models the needle-tissue interactions as a triangularly distributed load with superimposed uniform load (first order, $m = 1$). The input for Model 3 is also needle base force and torque.

A comparison between measured and estimated needle tip deflection path for Tissue 1, Tissue 2 and Tissue 3 is given in Fig. 7a, Fig. 7b and Fig. 7c, respectively. The average of the measured and estimated needle tip deflection for 6 trials is plotted along with the error between average estimated and measured tip deflections. Initially, up to a depth of approximately 50 mm, all models show a very similar performance as the estimation errors show only minor deviations among the models. At 50 mm depth, however, Model 1 starts to overestimate tip deflection followed by Model 2 at approximately 100 mm depth. Model 3 maintains the best accuracy up to an insertion depth of approximately 130 mm as the estimation error remains below 1 mm.

Table II presents the results of a two-sample t-test. The null hypothesis is that the mean of the measured deflection is equal to the mean of the estimated deflection over six trials. The variable r denotes that the null hypothesis must be rejected at the 5% significance level and $\bar{r}$ denotes that the null hypothesis can not be rejected. As the error of Model 1 and Model 2 increases during insertion, the null hypothesis must be rejected at higher insertion depths meaning that the model inaccuracy is statistically significant. Only Model 3 shows a high accuracy up to the final insertion depth such that the null hypothesis can not be rejected for all four considered insertion depths.

Table III gives the mean absolute error (MAE) between measured and estimated needle tip deflection for all models and tissue samples. As can be observed, the MAE is by far lowest for Model 3. For both Model 2 and Model 3, the

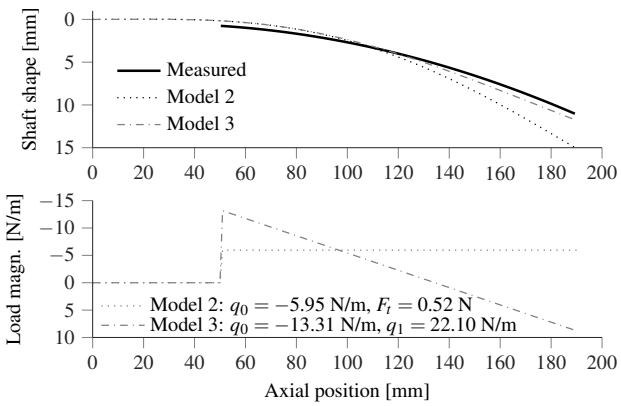

(a) Tissue 1

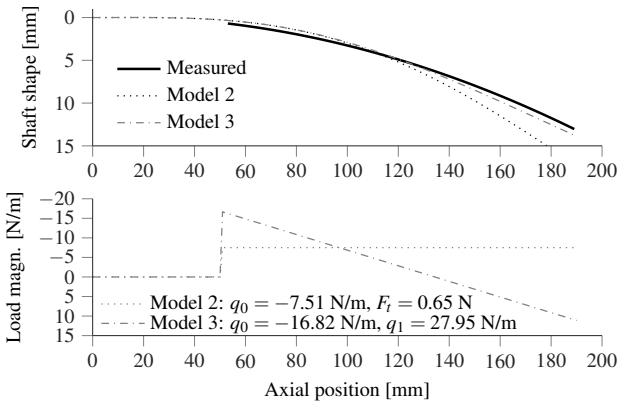

(b) Tissue 2

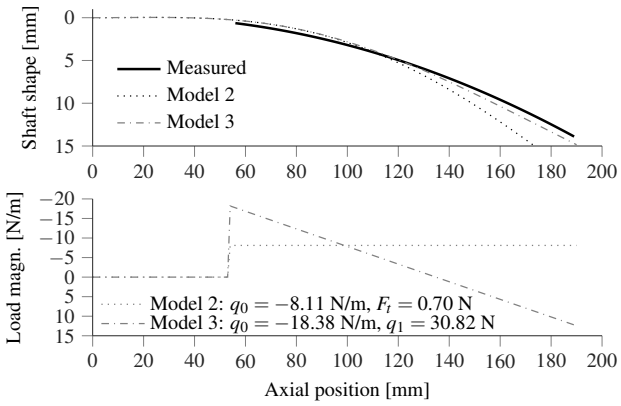

(c) Tissue 3

Fig. 8. The measured and estimated needle shaft shape at an insertion depth of 140 mm with estimates of Model 2 and Model 3 for (a) Tissue 1, (b) Tissue 2 and (c) Tissue 3. Insertion trial number six is plotted in the graphs for all tissue samples. The bottom plot shows the estimated loads for each model.

MAE remains below 1 mm while for Model 1, the MAE is significantly higher than 1 mm.

Fig. 8a, Fig. 8b and Fig. 8c show the needle deflection shapes for Tissue 1, Tissue 2 and Tissue 3, respectively. For all three tissues, the needle shaft shape at a final insertion depth of 140 mm is plotted. As expected, based on the observation in Fig. 7, the shape estimated by Model 3 follows the measured shape more closely than those estimated by Model 2. Moreover, the estimated load shapes shown in the bottom plots match the identified load shapes shown in Fig. 3.

D. Discussion

The needle tip deflection estimation results show that a more accurate needle tip deflection and shape estimation is in fact achieved with a first-order load distribution (proposed Model 3) as opposed to a zeroth-order distribution. The results also show that it is feasible to reduce the loads modeling needle-tissue interactions to only the distributed load while omitting the cutting induced point load F_t at the needle tip as the most precise estimate is obtained with Model 3.

The comparison between the estimation performance of Model 1 in which the uniformly distributed load is reduced to a point load, and models 2 and 3 shows that not reducing the distributed load to a point load results in better estimation performance. It should be noted that in [25], the phantom tissue samples are made from agar while in this work, the phantom tissues are made from gelatin as it better recreates the properties of biological tissue [28]. Therefore, the enhanced modeling approach introduced in this paper shows a better performance with more realistic phantom tissue (e.g. gelatin). The data provided in Table III further reinforces the above statements.

By including biological tissue (Tissue 3) in the experimental validation of the deflection estimate, it is shown that the newly introduced needle-tissue interaction model not only shows good performance with homogeneous phantom tissue but also with ex-vivo, non-homogeneous, multi-layer tissue.

A novelty with respect to previously proposed models is that the entire shape of the needle shaft (see Fig. 8) is estimated, not only the needle tip deflection. This is done through (11), where the deflection at any point along the needle can be evaluated. The plots in Fig. 8 show that the estimated needle shape for Model 3 matches the measured needle shape inside tissue closely, which further indicates that the needle-tissue interaction loads considered in Model 3 are representative of the physical loads occurring along the inserted needle shaft. Furthermore, in the bottom plots of Fig. 8, the provided load parameters identified by the estimator differ for each tissue sample, which shows that the model adapts to the difference in needle shape among the three tissue samples and hence to the difference in tissue stiffness.

It should be noted that for evaluating model performances, the deflection estimate is calculated after insertion when all the data is collected. This allows us to use the same insertion data for all compared models, which makes the model comparison more consistent. The average deflection estimate computation time is 0.56 milliseconds. Real-time deflection feedback sampling rates of up to 1 kHz are possible with this computation time, which is 50 times higher than image-based measurement. The code was implemented in MATLAB and executed on an AMD Phenom™ II X4 CPU with a frequency of 3.4 GHz. Much higher sampling rates can be achieved with a more recent CPU.

Overall, the newly proposed generalized quasi-static model for needle-tissue interaction in this work provides not only a means for needle deflection estimation but also a framework for the identification of needle-tissue interactions as shown in Section IV-A. It proposes a general and adaptive pseudo-static model that is capable of modeling a variety of loads. Section IV is only one example of applications for the proposed model.

VI. Conclusion & Future Work

The novel pseudo-static modeling framework for needle-tissue interactions presented in this work is applied to estimating the needle tip deflection and the needle shape during needle insertion into soft tissue. Experimental validation shows that the estimate obtained from the newly developed method is more accurate than previously proposed needle-tissue interaction models of similar type, in particular for greater insertion depths and for multi-layer and non-homogeneous tissue samples. The model is not only useful for deflection estimation but can also be applied to identify needle-tissue interactions. In prostate brachytherapy, a grid template is used to guide the needle. As the template absorbs most forces and moments caused by needle deflection, the force/torque readings at the needle base would be drastically limited. Thus, in order to make our method more applicable for prostate brachytherapy, our future work includes the adaptation of our deflection estimation method to incorporate a sensorized grid template with which forces and moments acting on the template are measured. Furthermore, as it can not be ruled out that the needle deflects outside of the assumed deflection plane during insertion, the deflection estimation also needs to be extended to estimate out-of-plane deflection. Moreover, incorporating friction effects, which contribute to deflection, could further enhance the model's physical and estimation accuracy. We are also planning to use the deflection estimate obtained from this model as deflection feedback for needle path control in our future work.

Acknowledgements

This work was supported by the Natural Sciences and Engineering Research Council (NSERC) of Canada under grant CHRP 446520, the Canadian Institutes of Health Research (CIHR) under grant CPG 127768, and by the Alberta Innovates - Health Solutions (AIHS) under grant CRIO 201201232.

References

[1] G. Wan, Z. Wei, L. Gardi, D. B. Downey, and A. Fenster, "Brachytherapy needle deflection evaluation and correction," *Medical Physics*, vol. 32, no. 4, p. 902, 2005.

[2] N. Abolhassani, R. V. Patel, and F. Ayazi, "Minimization of needle deflection in robot-assisted percutaneous therapy," *The International Journal of Medical Robotics and Computer Assisted Surgery*, vol. 3, no. 2, pp. 140–148, Jun. 2007.

[3] S. Badaan, D. Petrisor, C. Kim, P. Mozer, D. Mazilu, L. Gruionu, A. Patriciu, K. Cleary, and D. Stoianovici, "Does needle rotation improve lesion targeting?" *The international journal of medical robotics + computer assisted surgery : MRCAS*, vol. 7, no. 2, pp. 138–147, Jun. 2011.

[4] G. Fichtinger, A. Deguet, K. Masamune, E. Balogh, G. S. Fischer, H. Mathieu, R. H. Taylor, S. J. Zinreich, and L. M. Fayad, "Image overlay guidance for needle insertion in CT scanner," *IEEE Transactions on Biomedical Engineering*, vol. 52, no. 8, pp. 1415–1424, 2005.

[5] O. Gerovich, P. Marayong, and A. M. Okamura, "The effect of visual and haptic feedback on computer-assisted needle insertion," *Computer Aided Surgery*, vol. 9, no. 6, pp. 243–249, 2004.

[6] C. Rossa, J. Fong, N. Usmani, R. Sloboda, and M. Tavakoli, "Multiactuator Haptic Feedback on the Wrist for Needle Steering Guidance in Brachytherapy," *IEEE Robotics and Automation Letters*, vol. 1, no. 2, pp. 852–859, 2016.

[7] S. Xu, J. Kruecker, P. Guion, N. Glossop, Z. Neeman, P. Choyke, A. K. Singh, and B. J. Wood, "Closed-loop control in fused mr-trus image-guided prostate biopsy," in *Medical Image Computing and Computer-Assisted Intervention - MICCAI 2007*, ser. Lecture Notes in Computer Science. Berlin, Heidelberg: Springer, November 2007, vol. 4791, ch. 16, pp. 128–135.

[8] J. Hong, T. Dohi, M. Hashizume, K. Konishi, and N. Hata, "An ultrasound-driven needle-insertion robot for percutaneous cholecystostomy," *Phys. Med. Biol.*, vol. 49, no. 3, pp. 441–455, Jan. 2004.

[9] D. Glozman and M. Shoham, "Image-guided robotic flexible needle steering," *IEEE Transactions on Robotics*, vol. 23, no. 3, pp. 459–467, Jun. 2007.

[10] G. J. Vrooijink, M. Abayazid, S. Patil, R. Alterovitz, and S. Misra, "Needle path planning and steering in a three-dimensional non-static environment using two-dimensional ultrasound images," *The International Journal of Robotics Research*, 2014.

[11] M. Waine, C. Rossa, R. Sloboda, N. Usmani, and M. Tavakoli, "3D Needle Shape Estimation in TRUS-Guided Prostate Brachytherapy Using 2D Ultrasound Images," *IEEE Journal of Biomedical and Health Informatics*, 2015, in press.

[12] C. Rossa, R. Sloboda, N. Usmani, and M. Tavakoli, "Estimating needle tip deflection in biological tissue from a single transverse ultrasound image: application to brachytherapy," *International Journal of Computer Assisted Radiology and Surgery*, pp. 1–13, 2015.

[13] M. Waine, C. Rossa, R. Sloboda, N. Usmani, and M. Tavakoli, "Needle Tracking and Deflection Prediction for Robot-Assisted Needle Insertion Using 2D Ultrasound Images," *Journal of Medical Robotics Research*, vol. 01, no. 01, p. 1640001, 2016.

[14] C. Rossa, M. Khadem, R. Sloboda, N. Usmani, and M. Tavakoli, "Adaptive Quasi-Static Modelling of Needle Deflection During Steering in Soft Tissue," *IEEE Robotics and Automation Letters*, vol. 1, no. 2, pp. 916–923, 2016.

[15] A. Okamura, C. Simone, and M. O'Leary, "Force modeling for needle insertion into soft tissue," *IEEE Transactions on Biomedical Engineering*, vol. 51, no. 10, pp. 1707–1716, Oct. 2004.

[16] S. Misra, K. B. Reed, B. W. Schafer, K. T. Ramesh, and A. M. Okamura, "Mechanics of flexible needles robotically steered through soft tissue," *The International Journal of Robotics Research*, vol. 29, no. 13, pp. 1640–1660, Nov. 2010.

[17] R. Roesthuis, Y. V. Veen, A. Jahya, and S. Misra, "Mechanics of needle-tissue interaction," in *2011 IEEE/RSJ International Conference on Intelligent Robots and Systems (IROS)*. IEEE, Sep. 2011, pp. 2557–2563.

[18] A. Asadian, M. R. Kermani, and R. V. Patel, "An analytical model for deflection of flexible needles during needle insertion," in *2011 IEEE/RSJ International Conference on Intelligent Robots and Systems (IROS)*. IEEE, Sep. 2011, pp. 2551–2556.

[19] M. Abayazid, R. J. Roesthuis, R. Reilink, and S. Misra, "Integrating deflection models and image feedback for real-time flexible needle steering," *IEEE Transactions on Robotics*, vol. 29, no. 2, pp. 542–553, Apr. 2013.

[20] M. Abayazid, M. Kemp, and S. Misra, "3d flexible needle steering in soft-tissue phantoms using fiber bragg grating sensors," in *2013 IEEE International Conference on Robotics and Automation (ICRA)*. IEEE, May 2013, pp. 5843–5849.

[21] M. Khadem, C. Rossa, N. Usmani, R. S. Sloboda, and M. Tavakoli, "A Two-body Rigid/Flexible Model of Needle Steering Dynamics in Soft Tissue," *IEEE/ASME Transactions on Mechatronics*, 2016, in press.

[22] H. Kataoka, T. Washio, M. Audette, and K. Mizuhara, "A Model for Relations Between Needle Deflection, Force, and Thickness on Needle Penetration," in *Medical Image Computing and Computer-Assisted Intervention - MICCAI 2001*, ser. Lecture Notes in Computer Science. Berlin, Heidelberg: Springer, 2001, vol. 2208, ch. 115, pp. 966–974.

[23] N. Abolhassani and R. V. Patel, "Deflection of a Flexible Needle during Insertion into Soft Tissue," in *Engineering in Medicine and Biology Society, 2006. EMBS '06. 28th Annual International Conference of the IEEE*. IEEE, Aug. 2006, pp. 3858–3861, PMID: 17946584.

[24] T. Lehmann, M. Tavakoli, N. Usmani, and R. Sloboda, "Force-Sensor-Based Estimation of Needle Tip Deflection in Brachytherapy," *Journal of Sensors*, vol. 2013, pp. 1–10, 2013.

[25] T. Lehmann, C. Rossa, N. Usmani, R. Sloboda, and M. Tavakoli, "A virtual sensor for needle deflection estimation during soft-tissue needle insertion," in *2015 IEEE International Conference on Robotics and Automation (ICRA)*. IEEE, May 2015, pp. 1217–1222.

[26] J. M. Gere and S. P. Timoshenko, *Mechanics of Materials*. Boston, MA: Springer US, 1991.

[27] A. P. C. Choi and Y. P. Zheng, "Estimation of Young's modulus and Poisson's ratio of soft tissue from indentation using two different-sized indentors: Finite element analysis of the finite deformation effect," *Medical and Biological Engineering and Computing*, vol. 43, no. 2, pp. 258–264, 2005.

[28] A. Leibinger, A. E. Forte, Z. Tan, M. J. Oldfield, F. Beyrau, D. Dini, and F. y Baena, "Soft Tissue Phantoms for Realistic Needle Insertion: A Comparative Study," *Annals of Biomedical Engineering*, pp. 1–11, 2015.

Thomas Lehmann received the BSc degree in Medical Engineering in 2011 and the MSc degree in Biomedical Engineering in 2013, from the Hochschule Furtwangen University, Schwenningen, Germany.

He is currently working towards the PhD degree in Electrical and Computer Engineering at the University of Alberta, Edmonton, Canada. His research is focused on robotics-assisted needle insertion, and needle deflection sensing and control. Mr. Lehmann's research interests include medical robotics and sensor technologies.

Carlos Rossa received the Engineering and the M.Sc degrees in Mechatronics from the Ecole Nationale d'Ingenieurs de Metz, France, both in 2010, and earned the PhD degree in Mechatronics and Robotics from the University of Paris VI, Paris, France in 2013.

He is currently a postdoctoral research fellow with the Department of Electrical and Computer Engineering at the University of Alberta, Edmonton, Canada. Dr. Rossa's current research interests include the design and control of haptic interfaces, actuators and sensors technologies, mechatronics, and medical robotics.

Nawaid Usmani is an Associate Professor in the Department of Oncology, University of Alberta, Canada, and a radiation Oncologist at Cross Cancer Institute, Edmonton, Canada. He received his Bachelor of Arts & Science from McMaster University, Canada in 1998 and his Doctorate of Medicine from McMaster University in 2001.

Dr. Usmani's main focus on research is in prostate brachytherapy, including magnetic resonant imaging and PET imaging in the management of prostate cancer.

Ron S. Sloboda is a Professor in the Department of Oncology, University of Alberta, Canada. He received his BSc degree in Physics from the University of Manitoba, Canada, in 1974 and his PhD degree in Physics, Nuclear Theory from the University of Alberta, Canada, in 1979.

Dr. Sloboda's research interests are dosimetry and treatment planning for brachytherapy, including the design of clinical studies to obtain patient data that inform model-based dose calculation.

Mahdi Tavakoli is an Associate Professor in the Department of Electrical and Computer Engineering, University of Alberta, Canada. He received his BSc and MSc degrees in Electrical Engineering from Ferdowsi University and K.N. Toosi University, Iran, in 1996 and 1999, respectively. He received his PhD degree in Electrical and Computer Engineering from the University of Western Ontario, Canada, in 2005. In 2006, he was a post-doctoral researcher at Canadian Surgical Technologies and Advanced Robotics (CSTAR), Canada. In 2007-2008, he was an NSERC Post-Doctoral Fellow at Harvard University, USA.

Dr. Tavakoli's research interests broadly involve the areas of robotics and systems control. Specifically, his research focuses on haptics and teleoperation control, medical robotics, and image-guided surgery.